

Optical turbulence retrieval of heterogeneous media

Masaki Watabe,^{1,2,*} Joe Sakamoto,^{3,4,†} Hideaki Yoshimura,^{5,‡} Tomomi Nemoto,^{3,4} and Kazunari Kaizu^{1,6}

¹*Cell Modeling and Simulation Research Group, The Exploratory Research Center on Life and Living Systems, Okazaki, Aichi 444-8787, Japan*

²*Interdisciplinary Research Unit, National Institute for Basic Biology, Okazaki, Aichi 444-8585, Japan*

³*Biophotonics Research Group, The Exploratory Research Center on Life and Living Systems, Okazaki, Aichi 444-8787, Japan*

⁴*Division of Biophotonics, National Institute for Physiological Sciences, Okazaki, Aichi 444-8585, Japan*

⁵*School of Science, The University of Tokyo, 7-3-1 Hongo, Bunkyo-ku, Tokyo 113-0033, Japan*

⁶*Laboratory for Biologically Inspired Computing, RIKEN Center for Biosystems Dynamics Research, Kobe, Hyogo 650-0047, Japan*

(Dated: June 17, 2025)

Although the transport of intensity equation (TIE) can be used to reconstruct the spatial phase variations produced by samples such as magnetic materials and biological cells, the impact of complex refractive indices on quantitative phase imaging remains unexplored. To overcome this difficulty, we provide herein a more physically generalized TIE framework that enables the reconstruction of spatial variations in both refractive-index fluctuations and attenuation coefficients. We then demonstrate this method using bright-field microscopy imaging. The results reveal robust performance in retrieving heterogeneous optical structures within measurable parameter regions. Finally, we analyze the symmetry of the attenuation reversal in the TIE framework, thus revealing the invariant nature of the absorptive and scattering properties in the samples of interest.

Introduction. Teague’s seminal 1983 paper [1, 2] introduced a groundbreaking approach to the phase retrieval problem in optics. Unlike classical iterative methods, Teague proposed a direct, deterministic solution in the form of the transport of intensity equation (TIE), which relates phase gradients to intensity variations through a Green’s function. By measuring the intensity and its axial derivative along a longitudinal axis, it became possible to computationally deduce the spatial phase variations without ambiguity. In recent years, this technique has found extensive applications beyond its original microscopy context. It has been adapted for quantum state tomography, astronomical imaging, and particularly in ptychography for high-resolution material and biological studies [3–6]. Modern implementations often combine Teague’s core principles with machine learning approaches, especially deep neural networks, to accelerate convergence and improve robustness against noise [7–11].

Although Teague’s TIE formulation established an essential foundation for deterministic phase retrieval, a complementary phase transport equation emerges naturally from the same physical principles. When paired with the TIE, this phase transport equation provides a more comprehensive description of the evolution of the electromagnetic field. However, Teague’s original formulation primarily addresses wavefront propagation in free space or in homogeneous media with negligible scattering and absorption. In practical applications, light often traverses heterogeneous media with spatially varying refractive indices and nonnegligible attenuation coefficients. As light propagates through such media, it experiences both phase delays and amplitude modulations due to local variations in the optical properties, and the standard TIE framework cannot fully capture these complex interactions. A more physically accurate

model must account for how local medium properties—specifically complex refractive indices—affect both the amplitude and phase of the propagating wavefield, particularly in biological samples where structural heterogeneity is intrinsic to their function.

In this Letter, we modify Teague’s original mathematical description and derive a coupled set of transport equations that account for how the complex refractive indices in the samples of interest affect the propagation of a monochromatic plane wave. Such modified transport equations allow us to implement an algorithm to reconstruct the spatial variations of both the refractive-index fluctuations and the attenuation coefficients. We then demonstrate this method via bright-field microscopy imaging. The results lie within the statistically allowed 3σ (i.e., 99.7%) confidence level (or interval), reflecting robust reconstruction of heterogeneous optical structures within physically acceptable uncertainty bounds. Finally, we analyze the symmetry of the attenuation reversal in optical imaging. This symmetry verification is directly relevant to the invariance of the absorptive and scattering properties along the optical axis, thus providing physically valuable insights into the medium’s internal structure.

Theoretical scheme. For a specific wavelength λ in the intermediate field, the paraxial wave equation can be reformulated using the laws of energy conservation (i.e., the Helmholtz equation) and parametrized with a complex optical potential for heterogeneous media (see a complete discussion in Ref. [12]),

$$i \frac{\partial A}{\partial z} = \left[\frac{-1}{2kn_0} \nabla_{\perp}^2 - \frac{\partial}{\partial z} (\beta + i\alpha) \right] A \quad (1)$$

where ∇_{\perp} is the two-dimensional Nabla operator in the transverse direction [i.e., $\nabla_{\perp} = (\partial/\partial x, \partial/\partial y)$]. A is the

scalar complex amplitude of the wave function [i.e., $A = A(r_\perp, z)$]. kn_0 is the wave number in a space filled with the mean of refractive-index [i.e., $kn_0 = 2\pi n_0/\lambda$].

The complex optical potential is given by the axial derivatives of the functions $\alpha(r_\perp, z)$ and $\beta(r_\perp, z)$, representing the amplitude and phase variations, respectively, arising from the spatial distributions of the refractive-index fluctuation $\Delta n(r_\perp, z)$ and attenuation index $\kappa(r_\perp, z)$,

$$\frac{\partial \alpha}{\partial z} = kn_0 (1 + \Delta n) \kappa, \quad (2)$$

$$\frac{\partial \beta}{\partial z} = kn_0 \left(\Delta n - \frac{1}{2} \kappa^2 \right). \quad (3)$$

If the complex optical potential is set to zero, then Eq. (1) converges to the original form of the paraxial wave equation that describes longitudinal wave propagation through free space.

If the scalar complex amplitude of the paraxial wave function is $A(r_\perp, z) = \sqrt{I(r_\perp, z)} e^{i\phi(r_\perp, z)}$, then Eq. (1) produces a coupled set of transport equations where phase $\phi(r_\perp, z)$ and intensity $I(r_\perp, z)$ are correlated. The TIE can be derived from the imaginary part of the modified paraxial wave equation and written as

$$\frac{\partial I}{\partial z} = -\frac{1}{kn_0} \nabla_\perp \cdot (I \nabla_\perp \phi) - 2 \frac{\partial \alpha}{\partial z} I, \quad (4)$$

In contrast, from the real part, we can deduce the transport of phase equation (TPE),

$$\frac{\partial \phi}{\partial z} = \frac{\partial \beta}{\partial z} - \frac{1}{2kn_0} (\nabla_\perp \phi)^2 + \frac{1}{2kn_0} \frac{\nabla_\perp^2 \sqrt{I}}{\sqrt{I}}. \quad (5)$$

where the left-hand side is the axial phase derivative that propagates the phase along the z -axis, and the right-hand side is the phase variation in the transverse direction. Such phase variations consist of three terms: The $\partial \beta / \partial z$ term is the axial phase differentiations arising from the spatial fluctuation of the refractive and attenuation indices. The second term $(\nabla_\perp \phi)^2$ describes the nonlinear translational effects arising from the transverse phase gradients. Finally, the term $(\nabla_\perp^2 \sqrt{I}) / \sqrt{I}$ is the normalized fluctuation stemming from the convergent or divergent behavior (i.e., curvature) in the real part of the amplitude of the wave function. The derivation of the TPE is fully discussed in Sec. A of the Supplementary Material (SM) [13].

Reconstruction algorithm. We now develop a multifaceted approach that uses the distinct but complementary properties of the transport equations to systematically reconstruct the optical turbulence and interactions inherent in heterogeneous media. First, we assume a linear perturbation in the form of Eq. (4) along the longitudinal axis. For a specific parameter configuration of TIE imaging, a through-focus series of image intensities

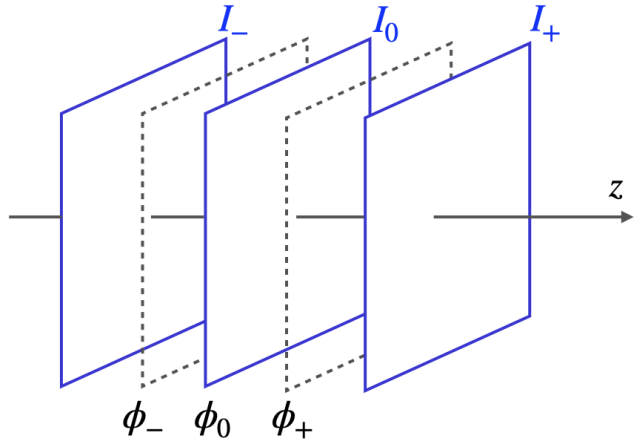


FIG. 1. Phase retrieval via TIE imaging typically involves a through-focus series of image intensities at three different z -positions, $I(z_0 - \Delta z)$, $I(z_0)$ and $I(z_0 + \Delta z)$. These images are then used to compute the axial intensity derivatives, which, when combined with the intensity distributions at the in-focus and half of the defocus z -positions, solves the TIE and reconstructs the phase distributions $\phi(z_0 - \Delta z/2)$, $\phi(z_0)$ and $\phi(z_0 + \Delta z/2)$.

at three different z -positions (i.e., I_0 and I_\pm in Fig. 1) can be represented in the form of

$$I_\pm \approx I_0 \mp \frac{\Delta z}{kn_0} \nabla \cdot [I_0 \nabla \phi_0] - 2I_0 \frac{\partial \alpha}{\partial z} \bigg|_{z_0} \Delta z \quad (6)$$

where Δz is the defocus distance along the z -axis, and ϕ_0 is the phase distribution at the in-focus z -position $z = z_0$ (see Fig. 1).

By leveraging the axial asymmetric component of Eq. (6), phase retrieval is performed to isolate the phase gradient terms from the intensity derivatives and attenuations along the longitudinal axis. The phase information at the in-focus and half-defocus axial-positions (i.e., z_0 and $z_0 \pm \Delta z/2$) can be computed by using retrieval algorithms such as the fast Fourier transform method [3, 14], providing a foundation for the subsequent characterization of the complex optical potential.

The intensity reduction parameter $\partial \alpha / \partial z$ is reconstructed by exploiting the axially symmetric component of Eq. (6), which captures how the wavefield's intensity attenuates during propagation due to the absorption and scattering in a medium. While the phase information (i.e., ϕ_0 and ϕ_\pm in Fig. 1) emerges from the axially asymmetric property of the TIE, we determine the phase-coupling parameter $\partial \beta / \partial z$ by using the TPE in conjunction with the phase derivative measurements along the axial axis, $(\phi_+ - \phi_-) / \Delta z$, effectively quantifying how local phase variations influence wavefront deformation. These intermediary representations serve as computational bridges, ultimately converting parameters into physically meaningful quantities: the spatially vary-

ing real and imaginary components of the complex refractive index,

$$\Delta n \approx \frac{\partial_z \beta / kn_0 + \frac{1}{2} (\partial_z \alpha / kn_0)^2}{1 - 2 (\partial_z \beta / kn_0)} \quad (7)$$

$$\mu = kn_0 \kappa = \frac{\partial_z \alpha}{1 + \Delta n} \quad (8)$$

where we assume $\Delta n^2 \sim 0$ and $\Delta n^3 \sim 0$ for weakly perturbed media, and ∂_z is the differential operator along the z -axis (i.e., $\partial/\partial z$). Thus, this multistep approach enables a robust reconstruction of both the refractive and attenuated properties from a minimal set of defocused intensity measurements (see the SM Sec. B for a full description), offering significant advantages over conventional phase reconstruction methods that assume the wavefront propagation in free space.

Reconstruction limits. For parameters configured for TIE imaging, we estimate the statistical and physical limits of the reconstruction algorithm. The statistical limits are primarily governed by the probability of an incident beam propagating through a complex refractive index, which determines the likelihood of the complex optical information being encoded into intensity variations. This probability must suffice to ensure reliable reconstruction, particularly as follows:

$$P(\Delta z) = \int \Phi(k) e^{-2kn_0(1+\Delta n)\kappa\Delta z} dk \quad (9)$$

where $\Phi(k)$ is the spectrum of the incident beam flux, normalized by $\int \Phi(k) dk = 1$. The exponential part comes from Fourier-transforming the transmission probability of an incident beam, exhibiting how different spatial frequency components of the incident beam are modulated during propagation through media with refractive and attenuation indices in a given pixel position. This probability distribution allows us to establish confidence intervals for the reconstructed optical parameters, typically expressed as a range within which the true values of the refractive and attenuation indices lie with a specified confidence level (e.g., 95%). These confidence intervals are critical for quantitatively evaluating the reliability of optical parameter reconstruction, particularly in regions where media properties in significant intensity reductions or refractive-index variations that approach the detection limits of the system.

For reliable data analysis and interpretation, we estimated the physical boundaries of the reconstruction algorithm. These constraints are governed by the parameter configuration for TIE imaging and the laws of photon counting, which establish the measurable range of refractive index variations,

$$\left(\frac{2\Delta x}{\pi\Delta z} \right)^2 < \left| \Delta n - \frac{1}{2}\kappa^2 \right| < 1 - \frac{1}{2}\kappa^2 \quad (10)$$

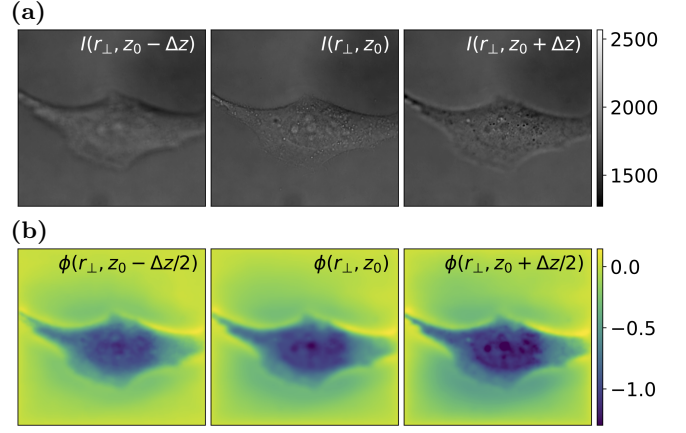


FIG. 2. The computational inputs of HeLa cells: (a) the image intensities (I_- , I_0 and I_+), and (b) the phases (ϕ_- , ϕ_0 and ϕ_+) reconstructed by using the GMGM.

where Δx is the pixel resolution of the detector. The lower bound is governed by the signal-to-noise ratio (SNR) of the detector's photon counting, which must exceed unity for meaningful reconstruction.

The physical lower bound represented in Eq. (10) particularly depends on the ratio between the lateral resolution Δx and the propagation distance Δz in the optical system. This ratio characterizes the minimum detectable phase gradient that can be measured through variations in intensity. When the spatial frequencies approach this limit, diffraction effects cause information loss in the measurements. As this ratio increases (due to poorer resolution or a decreased propagation distance), the minimum detectable variation in refractive-index increases quadratically, thereby reducing sensitivity to fine structural features. This establishes a fundamental physical boundary beyond which the phase information cannot be recovered regardless of the detector quality (see the SM Sec. C for the derivation).

Conversely, we expect the upper bound of the refractive-index fluctuation to be much less than unity ($\Delta n \ll 1$), ensuring that the linear approximations underlying the TIE formalism remain valid. If this condition is violated, the reconstruction results become increasingly inaccurate because of nonlinear effects not accounted for in the optical modeling. Above this threshold, noise dominates the measured intensity variations, rendering the extracted optical information nonphysical and potentially leading to artifact-laden reconstructions that misrepresent the true sample properties.

Reconstruction results. We demonstrate our approach using two distinct sample types: a microlens array (MLA) sample [15] with well-defined optical properties and HeLa cells as a complex biological specimens. The experiments were done using a bright-field imaging system equipped with a laser-scanning confocal microscope [see Fig. S1(a) for the optical path] [16]. The full results

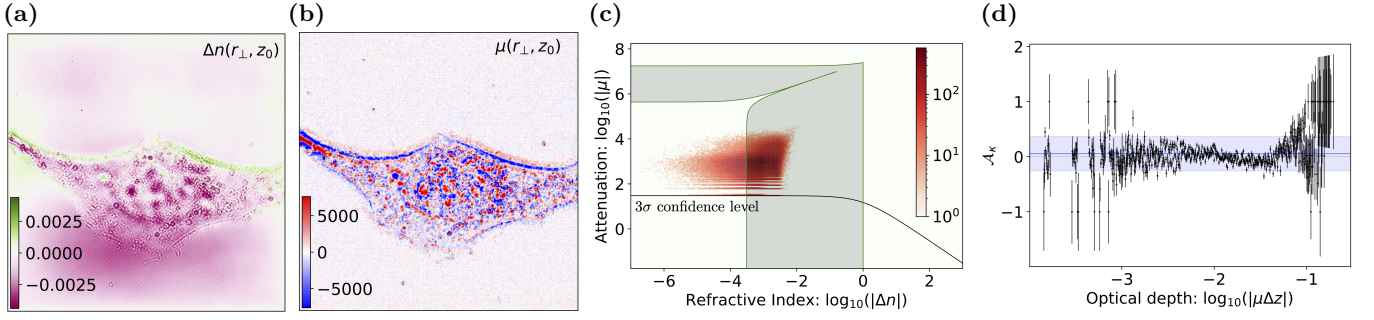


FIG. 3. Results for HeLa cells: (a) Spatial distribution of refractive-index fluctuations $\Delta n(r_{\perp}, z_0)$ and (b) attenuation coefficients $\mu(r_{\perp}, z_0)$. The sign of the $\mu(r_{\perp}, z_0)$ indicates forward and backward wave propagations along the z -axis. (c) Correlation patterns between $\Delta n(r_{\perp}, z_0)$ and $\mu(r_{\perp}, z_0)$. The black solid line is the 3σ confidence level. The green area is the physical boundaries given by Eq. (10). (d) Measured value of the asymmetry \mathcal{A}_{κ} in bins of the optical depth $\log_{10} |\mu\Delta z|$. The blue line and bands are the statistical average and the root mean squared (RMS) value, respectively. Dashed line represents $\mathcal{A}_{\kappa} = 0$.

are given in the SM Sec. D.

To image HeLa cells, a through-focus series of intensity distributions was acquired at three distinct z -positions to serve as the inputs into our computational approach [see Figs. 2(a)]. To quantify the attenuation effects throughout the sample, the intensity reduction parameter $\partial\alpha/\partial z$ is recovered using the axially symmetric component of the TIE [see Figs. S5(c)]. The algorithm extracts the phase distributions [see Fig. 2(b)] by applying the geometric multigrid method (GMGM) [17–20], analyzing the phase-coupling parameter $\partial\beta/\partial z$ via the TPE combined with the axial phase derivative measurements $(\phi_+ - \phi_-)/\Delta z$ [see Figs. S5(d)]. These intermediary parameters are finally converted into physically meaningful quantities: the spatial variations of the refractive-index fluctuations Δn and attenuation coefficients μ [see Figs. 3(a) and 3(b)]. In particular, Figs. 3(c) shows the correlation pattern between Δn and μ , revealing 65,055 events (24.82%) that fall outside the measurable parameter region (i.e., green area).

We also implemented our reconstruction approach for the MLA sample to verify its ability to capture the distinctive optical properties of nonbiological components. The histograms of the refractive-index fluctuation Δn and attenuation coefficients μ reveal multiple characteristic peaks [see Figs. S3(e) and S3(f)], which may be attributed to the inherent structural properties of the MLA sample, showing that the algorithm is sensitive to discrete optical features within the measurable parameter regions. When examining the correlation patterns between Δn and μ [see Fig. S3(g)], we observe periodic stripe artifacts that likely originate from the laser-scanning of the confocal microscope system, providing insight into uncertainties in the measurement process. Notably, while the microlens pattern appears distinctly in the attenuation coefficient distributions [see Figs. S3(f)], the refractive-index fluctuations display a relatively flatter distribution with no discernible lens patterns [see Figs. S3(e)]. This difference between the optical parameters demonstrates

the algorithm’s capability to distinguish various optical properties within structured samples. These results from the MLA sample reliably verify the performance of our computational approach, confirming its ability to accurately reconstruct complex optical characteristics in non-biological samples.

For bright-field imaging of HeLa cell membranes, we used a wide-field microscope illuminated by a xenon lamp [see Figs. S1(b) for the optical path]. The system provided a broader spectral profile with multiple illumination peaks [21] in the wavelength range of a 525/30 nm bandpass filter. A through-focus series of image intensities was acquired at three distinct z -positions, although the broader spectral characteristics of the xenon source required additional computational processing to account for the wavelength-dependent optical responses. Despite this spectral complexity, the proposed approach extracted the intensity reduction parameter and recovered the phase distributions by using the GMGM. Crucially, the analysis of the phase-coupling parameter reveals membrane-specific optical signatures, with the converted refractive-index fluctuations and attenuation coefficients exhibiting a slightly narrower range of 3σ confidence interval compared with the results from laser illumination (see Figs. S2). Figures S7 and S8 display these parameter distributions across the HeLa cell membrane, mapping the Δn - μ correlation patterns within the reconstruction limits [see Fig. S8(g)]. These results demonstrate the versatility of our computational approach across different illumination modalities.

Symmetry in wave propagation. The optical attenuation in the paraxial wave equation demonstrates a fundamental symmetry that governs wave propagation in heterogeneous media. This symmetry categorizes the propagation modes into transmission and reflection based on the sign of the attenuation index, with positive values indicating forward propagation and negative values indicating backward propagation. When the wave propagation probability remains unchanged by directional inversion

($\kappa \mapsto -\kappa$), identical diffraction patterns emerge regardless of the direction, demonstrating optical isotropy in the medium. Conversely, asymmetry emerges in nonreciprocal media where optical isotropy is disrupted, causing observable differences in the diffraction patterns and intensity distributions between forward and backward propagation.

The optical invariance in TIE imaging can be verified using the asymmetry of the probability functions propagating in the forward and backward directions,

$$\mathcal{A}_\kappa = \frac{\mathcal{P}(+\kappa) - \mathcal{P}(-\kappa)}{\mathcal{P}(+\kappa) + \mathcal{P}(-\kappa)} \quad (11)$$

where $\mathcal{P}(\pm\kappa)$ is the wave propagation probability, which depends on the sign of the attenuation index. If $\mathcal{A}_\kappa = 0$, then the wave propagation probabilities are conserved between the forward and backward directions; otherwise, the symmetry is broken in TIE imaging. Figure 3(d) shows the propagation asymmetry \mathcal{A}_κ to be nearly zeros with respect to the optical depth, representing an equivalent relation of the probability densities between forward and backward wave propagation. This result implies the approximate preservation of the invariance of the attenuate property in HeLa cell imaging. However, for the other samples, the invariance is broken because the propagation asymmetry is the nonzero: $\mathcal{A}_\kappa \neq 0$ (see the SM Sec. D.3 for the full results).

Conclusion. This study extends Teague’s TIE framework by incorporating the effects of complex light-matter interactions in heterogeneous media. This fundamental advancement in optical modeling enables the reconstruction of spatial variations for both refractive-index fluctuations and attenuation coefficients. The coupled transport equations derived and validated across multiple imaging modalities robustly capture fine structural details and optical characteristics previously obscured by traditional TIE implementations. Further analysis of the attenuation phenomena reveals the invariant nature of the absorptive and scattering properties along the optical axis. This comprehensive approach to bridging a physical gap in phase retrieval methodology opens new approaches for both basic research and applied technologies, potentially transforming how complex media structures are characterized and understood across multiple scientific disciplines. The integration of these proposed methods into modern computational techniques further suggests significant potential for next-generation imaging systems that would be capable of revealing deeper insights into the medium’s internal structures.

Data availability. The data that support the findings of this article are openly available [22].

Acknowledgments. The authors express their sincere gratitude to Masayuki Hattori, Naru Yoneda, and Osamu Matoba for their invaluable guidance and support throughout this research. This work was supported by the Japan Society for the Promotion of Sci-

ence (JSPS) KAKENHI Grant Numbers JP20H05891, JP20K21836, JP21H05605, JP22H04926, JP23K17364, and JP23K26795. Additional support was provided by the Asahi Glass Foundation, and by the Joint Research of the Exploratory Research Center on Life and Living Systems (ExCELLS) through the ExCELLS Encouragement Research Program for Young Scientists.

* Corresponding author: m-watabe@nibb.ac.jp

† Contributed equally with the first author; This author performed experiments.

‡ This author performed experiments.

- [1] M. R. Teague, Deterministic Phase Retrieval: a Green’s Function Solution., Journal of the Optical Society of America **73**, 1434–1441 (1983).
- [2] M. R. Teague, Irradiance Moments: Their Propagation and Use for Unique Retrieval of Phase., J Opt Soc Am **V 72**, 1199–1209 (1982).
- [3] M. Mitome, Transport of intensity equation method and its applications, Microscopy **70**, 69–74 (2021).
- [4] C. Zuo, J. Li, J. Sun, Y. Fan, J. Zhang, L. Lu, R. Zhang, B. Wang, L. Huang, and Q. Chen, Transport of intensity equation: a tutorial, Optics and Lasers in Engineering **135**, 106187 (2020).
- [5] S. K. Rajput, O. Matoba, M. Kumar, X. Quan, Y. Awatsuji, Y. Tamada, and E. Tajahuerce, Multi-Physical Parameter Cross-Sectional Imaging of Quantitative Phase and Fluorescence by Integrated Multimodal Microscopy, IEEE Journal of Selected Topics in Quantum Electronics **27**, 1–9 (2021).
- [6] S. K. Rajput, M. Kumar, X. Quan, M. Morita, T. Furuyashiki, Y. Awatsuji, E. Tajahuerce, and O. Matoba, Three-dimensional fluorescence imaging using the transport of intensity equation, Journal of Biomedical Optics **25**, 1 (2019).
- [7] V. Thapa, A. S. Galande, G. H. P. Ram, and R. John, TIE-GANs: single-shot quantitative phase imaging using transport of intensity equation with integration of GANs, Journal of Biomedical Optics **29**, 1–18 (2024).
- [8] K. Wang, L. Song, C. Wang, Z. Ren, G. Zhao, J. Dou, J. Di, G. Barbastathis, R. Zhou, J. Zhao, and E. Y. Lam, On the use of deep learning for phase recovery, Light: Science and Applications **13**, 10.1038/s41377-023-01340-x (2024), arXiv:2308.00942.
- [9] X. Wu, Z. Wu, S. C. Shanmugavel, H. Z. Yu, and Y. Zhu, Physics-informed neural network for phase imaging based on transport of intensity equation, Optics Express **30**, 43398 (2022).
- [10] X. Wu, S. C. Shanmugavel, and Y. Zhu, Transport of Intensity Equation based Phase Retrieval Using Deep Transfer Learning, Optics InfoBase Conference Papers **2022**, 3–4 (2022).
- [11] K. Wang, J. Di, Y. Li, Z. Ren, Q. Kemao, and J. Zhao, Transport of intensity equation from a single intensity image via deep learning, Optics and Lasers in Engineering **134**, 106233 (2020).
- [12] M. Watabe, Y. Hirano, A. Iwane, O. Matoba, and K. Takahashi, Optical dispersions through intracellular inhomogeneities, Phys. Rev. Research **022043**, 1–6

- (2023).
- [13] See Supplemental Material at (URL will be inserted by publisher) for further details.
 - [14] D. Paganin and K. A. Nugent, Noninterferometric phase imaging with partially coherent light, *Physical Review Letters* **80**, 2586–2589 (1998).
 - [15] MLA300-14AR-M- $\phi 1''$ Mounted Lens Array – Thorlabs, <https://www.thorlabs.co.jp/thorproduct.cfm?partnumber=MLA300-14AR-M>, accessed: 2025-05-01.
 - [16] N. Yoneda, J. Sakamoto, T. Tomoi, T. Nemoto, Y. Tamada, and O. Matoba, Transport-of-intensity phase imaging using commercially available confocal microscope, *J. Biomed. Opt.* **29**, 116002 (2024).
 - [17] S. Mazumder, *Numerical Methods for Partial Differential Equations: Finite Difference and Finite Volume Methods.*, 1st ed. (Academic Press, 2016).
 - [18] B. Xue and S. Zheng, Phase retrieval using the transport of intensity equation solved by the FMG-CG method, *Optik (Stuttg.)* **122**, 2101–2106 (2011).
 - [19] S. V. Pinhasi, R. Alimi, L. Perelmutter, and S. Eliezer, Topography retrieval using different solutions of the Transport Intensity Equation, *Optical Society of America* **27**, 2285–2292 (2010).
 - [20] W. H. Press, S. A. Teukolsky, W. T. Vetterling, and B. P. Flannery, *Numerical Recipes in C: The Art of Scientific Computing.*, 2nd ed. (Cambridge University Press, 1992).
 - [21] Xenon Arc Light Sources – Thorlabs, https://www.thorlabs.com/newgrouppage9.cfm?objectgroup_ID=13016, accessed: 2025-04-10.
 - [22] Data is available at Zenodo, <https://doi.org/10.5281/zenodo.15589385>.
 - [23] M. Watabe, Physical constraints to phase retrieval using the transport of intensity equation in fluorescence microscopy imaging., presented at the 1st Conference for Sensing and Imaging Through Scattering and Fluctuating Field in Biology, Telecommunication and Astronomy (SI-Thru2022), dated: Apr. 19-22, 2022 at Pacifico Yokohama, Japan.
 - [24] T. Yamada, H. Yoshimura, R. Shimada, M. Hattori, M. Eguchi, T. K. Fujiwara, A. Kusumi, and T. Ozawa, Spatiotemporal analysis with a genetically encoded fluorescent RNA probe reveals TERRA function around telomeres, *Scientific Reports* **6**, 1–13 (2016).

Supplemental Material

A. Derivation of the TPE

Separating the paraxial wave equation [i.e., Eq. (1) in the main text] into the real and imaginary sections, the TIE can be derived in the imaginary part (see the Sec. A.1 of the Supplementary Material in Ref. [12] for derivation). Conversely, the TPE can be derived in the real part and its derivation is given as follows.

In the real part of the paraxial wave equation,

$$\begin{aligned}
& \text{Re} \left[\nabla_{\perp}^2 A + 2kn_0 i \frac{\partial A}{\partial z} + 2kn_0 \frac{\partial}{\partial z} (\beta + i\alpha) A \right] = 0 \\
& \text{Re} \left[\nabla_{\perp}^2 \sqrt{I} e^{i\phi} + 2kn_0 i \frac{\partial}{\partial z} \sqrt{I} e^{i\phi} + 2kn_0 \frac{\partial}{\partial z} (\beta + i\alpha) \sqrt{I} e^{i\phi} \right] = 0 \\
& \text{Re} \left[\nabla_{\perp}^2 \sqrt{I} e^{i\phi} + 2kn_0 i \left(\frac{\partial \sqrt{I}}{\partial z} e^{i\phi} + \sqrt{I} \frac{\partial e^{i\phi}}{\partial z} \right) \right] + 2kn_0 \frac{\partial \beta}{\partial z} \sqrt{I} e^{i\phi} = 0 \\
& \text{Re} \left[\nabla_{\perp}^2 \sqrt{I} e^{i\phi} + 2kn_0 i \sqrt{I} \frac{\partial e^{i\phi}}{\partial z} \right] + 2kn_0 \frac{\partial \beta}{\partial z} \sqrt{I} e^{i\phi} = 0 \\
& \text{Re} \left[\nabla_{\perp}^2 \sqrt{I} e^{i\phi} \right] - 2kn_0 \sqrt{I} \frac{\partial \phi}{\partial z} e^{i\phi} + 2kn_0 \frac{\partial \beta}{\partial z} \sqrt{I} e^{i\phi} = 0 \\
& \text{Re} \left[(\nabla_{\perp}^2 \sqrt{I}) e^{i\phi} + 2(\nabla_{\perp} \sqrt{I}) (\nabla_{\perp} e^{i\phi}) + \sqrt{I} (\nabla_{\perp}^2 e^{i\phi}) \right] - 2kn_0 \sqrt{I} \frac{\partial \phi}{\partial z} e^{i\phi} + 2kn_0 \frac{\partial \beta}{\partial z} \sqrt{I} e^{i\phi} = 0 \\
& \left[\nabla_{\perp}^2 \sqrt{I} - \sqrt{I} (\nabla_{\perp} \phi)^2 \right] - 2kn_0 \sqrt{I} \frac{\partial \phi}{\partial z} + 2kn_0 \sqrt{I} \frac{\partial \beta}{\partial z} = 0
\end{aligned} \tag{S1}$$

Divided by $2kn_0 \sqrt{I}$, we can deduce the TPE,

$$\frac{\partial \phi}{\partial z} = \frac{\partial \beta}{\partial z} - \frac{1}{2kn_0} (\nabla_{\perp} \phi)^2 + \frac{1}{2kn_0} \frac{\nabla_{\perp}^2 \sqrt{I}}{\sqrt{I}} \tag{S2}$$

where the axial derivative of $\alpha(r_{\perp}, z)$ vanishes through this modification.

The last term in the Eq. (S2) can be rewritten as follows.

$$\frac{\nabla_{\perp}^2 \sqrt{I}}{\sqrt{I}} = \frac{1}{\sqrt{I}} \nabla_{\perp} \cdot \left(\frac{\nabla_{\perp} I}{2\sqrt{I}} \right) = \frac{\sqrt{I} (\nabla_{\perp}^2 I) - (\nabla_{\perp} \sqrt{I}) (\nabla_{\perp} I)}{2I\sqrt{I}} = \frac{2I (\nabla_{\perp}^2 I) - (\nabla_{\perp} I)^2}{4I^2}$$

Inserting this back to the Eq. (S2), the TPE can be also written in the form of

$$\frac{\partial \phi}{\partial z} = \frac{\partial \beta}{\partial z} - \frac{1}{2kn_0} (\nabla_{\perp} \phi)^2 + \frac{1}{4kn_0} \left(\frac{\nabla_{\perp}^2 I}{I} \right) - \frac{1}{8kn_0} \left(\frac{\nabla_{\perp} I}{I} \right)^2. \tag{S3}$$

B. Reconstruction method

Our reconstruction algorithm, developed to systematically recover optical turbulence and interactions in heterogeneous media, consists of four sequential steps:

- (1) As the first step of our linear perturbation approach along the longitudinal axis, we reconstruct the phase distribution ϕ_0 at the in-focus position by utilizing the axial asymmetric component of the Eq. (3) in the main text:

$$\frac{I_+ - I_-}{2\Delta z} \approx -\frac{1}{kn_0} \nabla \cdot [I_0 \nabla \phi_0] \quad (\text{S4})$$

where I_0 and I_{\pm} are the inputs of image intensities at the in-focus (z_0) and defocus positions ($z_0 \pm \Delta z$). This differential equation represents a Poisson equation that we solve using a geometric multigrid method (GMGM) [17–19, 23]. The multigrid approach provides efficient numerical solutions by operating on multiple resolution levels simultaneously, which significantly accelerates convergence compared to single-grid iterative methods. Our implementation employs a V-cycle scheme with Gauss-Seidel relaxation, which effectively handles both low and high spatial frequency components of the phase distribution while maintaining computational efficiency for large datasets. This approach is particularly advantageous for handling the boundary conditions and non-uniformities in intensity that are common in experimental data.

Also, we apply the same GMGM technique to retrieve phase distributions at the half-defocus positions ϕ_{\pm} using

$$\frac{I_{\pm} - I_0}{\Delta z} \approx -\frac{1}{kn_0} \nabla \cdot [I_{\pm 1/2} \nabla \phi_{\pm}] \quad (\text{S5})$$

where the intensity at half-defocus positions is estimated as $I_{\pm 1/2} = (I_0 + I_{\pm})/2$.

- (2) The intensity reduction parameter $\partial\alpha/\partial z$ is extracted by leveraging the axial symmetric component of the Eq. (6) in the main text:

$$\left. \frac{\partial\alpha}{\partial z} \right|_{z_0} \approx \frac{I_+ + I_- - 2I_0}{-4\Delta z I_0} \quad (\text{S6})$$

This parameter captures how the wavefield's intensity attenuates during propagation due to absorptive and scattering properties of the medium.

- (3) The phase-coupling parameter $\partial\beta/\partial z$ is computed by utilizing the TPE together with axial phase derivatives $\partial\phi/\partial z \approx (\phi^+ - \phi^-)/\Delta z$:

$$\left. \frac{\partial\beta}{\partial z} \right|_{z_0} \approx \frac{\phi_+ - \phi_-}{\Delta z} + \frac{1}{2kn_0} [\nabla_{\perp} \phi_0]^2 - \frac{1}{2kn_0} \frac{\nabla_{\perp}^2 \sqrt{I_0}}{\sqrt{I_0}} \quad (\text{S7})$$

This intermediary parameter effectively quantifies how local phase variations influence wavefront deformation during propagation.

- (4) Finally, the intermediary parameters $\partial\alpha/\partial z$ and $\partial\beta/\partial z$ are converted into physically meaningful quantities: the spatial distributions of refractive-index fluctuation and attenuation coefficients. The conversion functions are given by the Eq. (4)-(5) in the main text.

These transformations establish a direct link between measurable wavefield properties (intensity and phase) and the fundamental optical properties of the medium (refractive index and attenuation), enabling comprehensive characterization of heterogeneous optical media from a minimal set of through-focus measurements.

C. Reconstruction limits

The physical lower bound of the reconstruction method is fundamentally governed by the signal-to-noise ratio (SNR) of the detector's photon counting capability, which must exceed unity for meaningful reconstruction. This constraint emerges through a systematic two-stage derivation process.

First, we establish the lower bound for TIE-based phase retrieval. The fundamental constraint emerges from the requirement that intensity differences ΔI between the defocus image distances $2\Delta z$ must exceed the shot noise limit,

$$\Delta I = \left| -\frac{1}{kn_0} \int_{z_0-\Delta z}^{z_0+\Delta z} \nabla \cdot [I \nabla \phi] dz \right| > \sqrt{I(z_0) + I_{bg}} \quad (\text{S8})$$

where Δz and kn_0 are the defocus lateral distance and the wave number of signaling photons in the mean refractive index field, respectively. I_{bg} is intensity distributions in background.

For the sake of simplicity, we assume constant image intensity (i.e., $I_0 = \text{const}$) and sinusoidal phase distributions [i.e., $\phi = \phi_0 \sin(k_x x) k_z (z - z_0)$]. This constraint translates directly into a minimum detectable phase amplitude. In this assumption, we modify the Eq. (S8) to find that the minimum detectable phase variation,

$$|\phi| > \phi_{min} = \frac{kn_0 \sqrt{I_0 + I_{bg}}}{\Delta z k_x^2 I_0} = \frac{kn_0 \Delta z}{SNR} \left(\frac{2\Delta x}{\pi \Delta z} \right)^2 \quad (\text{S9})$$

where we assume the minimum spatial frequency $k_x = 2\pi/4\Delta x$ for phase signal detection. Further details are discussed in Ref. [23].

Building upon this foundation, we then derive the lower limit for the β -derivative intermediary function. Substituting our sinusoidal phase assumption and constant intensity to the TPE [i.e., Eq. (5) in the main text], we obtain

$$\begin{aligned} \frac{\partial \beta}{\partial z} &= \frac{\partial \phi}{\partial z} + \frac{1}{2kn_0} (\nabla_{\perp} \phi)^2 - \frac{1}{2kn_0} \frac{\nabla_{\perp}^2 \sqrt{I}}{\sqrt{I}} \\ &= \phi_0 \sin(k_x x) k_z + \frac{1}{2kn_0} (k_x \phi_0 \cos(k_x x) k_z \Delta z)^2 - \frac{1}{2kn_0} \frac{\nabla_{\perp}^2 \sqrt{I_0}}{\sqrt{I_0}} \\ &= \frac{\phi_0 \sin(k_x x) k_z \Delta z}{\Delta z} + \frac{1}{2kn_0} (k_x \phi_0 k_z \Delta z)^2 (1 - \sin^2(k_x x)) \\ &= \frac{\phi}{\Delta z} + \frac{1}{2kn_0} (k_x \phi_0 \sin(k_x x) k_z \Delta z)^2 \left(\frac{1}{\sin^2(k_x x)} - 1 \right) \\ &= \frac{\phi}{\Delta z} + \frac{1}{2kn_0} (k_x \phi)^2 \left(\frac{1}{\sin^2(k_x x)} - 1 \right) \end{aligned} \quad (\text{S10})$$

Inserting the Eq. (S9) into the Eq. (3), the β -derivative intermediary parameter can be limited as follows.

$$\left| \frac{\partial \beta}{\partial z} \right| > \frac{\phi^{min}}{\Delta z} + \frac{1}{2kn_0} (k_x \phi^{min})^2 \left(\frac{1}{\sin^2(k_x x)} - 1 \right) \xrightarrow{0} \quad (\text{S11})$$

where the nonlinear term vanishes as $\sin^2(k_x x) \rightarrow 1$. Dividing by kn_0 and setting $SNR = 1$ at observable minimum, we systematically arrive at the final constraint:

$$\left| \Delta n - \frac{1}{2} \kappa^2 \right| > \left(\frac{2\Delta x}{\pi \Delta z} \right)^2 \quad (\text{S12})$$

This derived physical lower bound characterizes the fundamental limit where spatial frequencies approach the critical diffraction threshold, causing irreversible information loss in the measurements. As the $\Delta x/\Delta z$ ratio increases—either due to poorer spatial resolution or decreased propagation distance—the minimum detectable refractive index variation increases quadratically, thus significantly reducing the method's sensitivity to fine structural features within the sample.

D. Analysis

D.1. Microscopy configuration

Configuration details for bright-field imaging systems are described as follows.

- (1) Laser-scanning confocal microscope [16]: Bright-field imaging was performed using a Nikon A1 Rei confocal system equipped with a PlanApo-VC 60 \times water-immersion objective lens (NA = 0.45; Olympus, Tokyo, Japan) at room temperature. As illustrated in Figure S1(a), the laser excitation beam is directed through a series of relay optics and mirrors to a dichroic mirror (DM), which reflects the beam into the objective lens and focuses it onto the physical and biological samples. The transmitted light followed by an aperture stop and field stop to spatially filter out-of-focus light is then relayed to a photodetector without a pinhole, allowing efficient signal collection while maintaining axial resolution through the optical filtering components.
 - Physical sample: The MLA300-14AR-M, a precision-fabricated microlens array from Thorlabs [15], was employed for testing the reconstruction performance. This array consists of a 10 \times 10 mm² fused silica substrate patterned with square plano-convex microlenses (295 μ m side length, 300 μ m pitch) arranged in a regular square grid. The lenslets were fabricated using photolithographic processes to ensure high positional accuracy and shape uniformity. A broadband anti-reflection (AR) coating optimized for the 400-900 nm wavelength range was applied, reducing surface reflectivity to below 1%. The array provides an effective focal length of 14.6 mm and a fill factor of approximately $\sim 96.7\%$, enabling efficient optical coupling. For experimental integration, the microlens array was housed in a $\phi 1"$ mount (25.4 mm diameter, 3.5 mm thickness) compatible with standard optomechanical components.
Parameters: wavelength of emission light, $\lambda = 488$ nm; defocus distance, $\Delta z = 100$ μ m; the scanning pitch, 0.621 μ m; magnification, $\times 10$; image pixel length, $\Delta x = \Delta y = 2.49$ μ m; total number of z-stack images, 41 image took 19min; image size, 1024 \times 1024 pixels; beam flux, $\Phi(k) = \delta(k - k_\lambda)$; and see Figure S2(a) for parameter allowed region in the $\Delta n(r_\perp, z_0)$ - $\mu(r_\perp, z_0)$ spaces.
 - Biological sample: HeLa cells (RCB0007, RIKEN Cell Bank, Tsukuba, Japan) were cultured under standard conditions. (..... more)
Parameters: wavelength of emission light, $\lambda = 488$ nm; defocus distance, $\Delta z = 200$ nm; image pixel length, $\Delta x = \Delta y = 0.138$ μ m; total number of z-stack images, 31 frames; image size, 512 \times 512 pixels; beam flux, $\Phi(k) = \delta(k - k_\lambda)$; and see Figure S2(b) for parameter allowed region in the $\Delta n(r_\perp, z_0)$ - $\mu(r_\perp, z_0)$ spaces.
- (2) Wide-field microscope: Bright-field observation experiments were conducted using home-built objective-type total internal reflection fluorescence microscopes (TIRFM) based on inverted microscopes (IX81; Olympus Corp.) [24]. As illustrated in Fig. S1(b), illumination was provided by a Xenon lamp (SLS401 Light Source with Xenon Arc Lamp for 240-2400 nm, 5800 K, Thorlabs) [21], with the beam first collimated and then filtered through a bandpass excitation filter (BF 525/30, Semrock Inc.) to select the desired wavelength range. The light was then reflected by a dichroic mirror and directed toward the biological sample (i.e., HeLa cells) through a high numerical aperture oil-immersion objective lens (100x, NA 1.49; Olympus Corp.). After interacting with the sample, the transmitted light was collected by the same objective and passed through an emission optical train that included a second dichroic mirror (DM R561, Semrock Inc.) and an emission bandpass filter (BF 525/50, Semrock Inc.). The filtered emission signal was finally focused onto an electron-multiplying CCD (EMCCD) camera (ImagEM; Hamamatsu Photonics Inc.) for image acquisition.
 - Biological sample: HeLa cells (???????, Japan) were cultured under standard conditions. (..... more)
Parameters: wavelength of emission light, $\lambda = 525$ nm; defocus distance, $\Delta z = 5$ μ m; image pixel length, $\Delta x = \Delta y = 80$ nm; total number of z-stack images, 41 frames; and image size, 512 \times 512 pixels; beam flux, $\Phi(k) = \Phi_{X_e}$ [21]; and see Figure S2(c) for parameter allowed region in the $\Delta n(r_\perp, z_0)$ - $\mu(r_\perp, z_0)$ spaces.

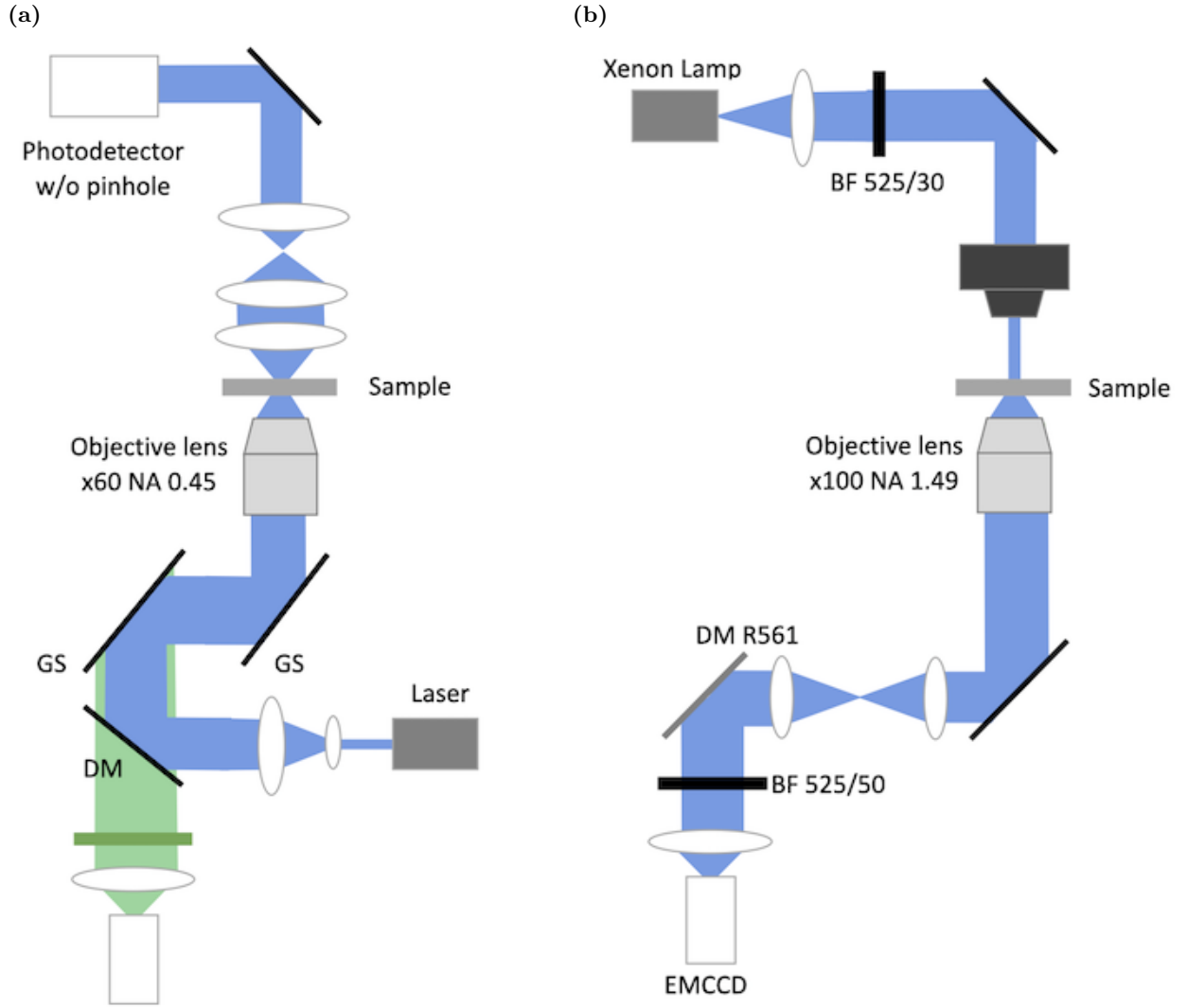


FIG. S1. Optical path for the bright-field imaging systems: (a) laser-scanning confocal microscope and (b) wide-field microscope.

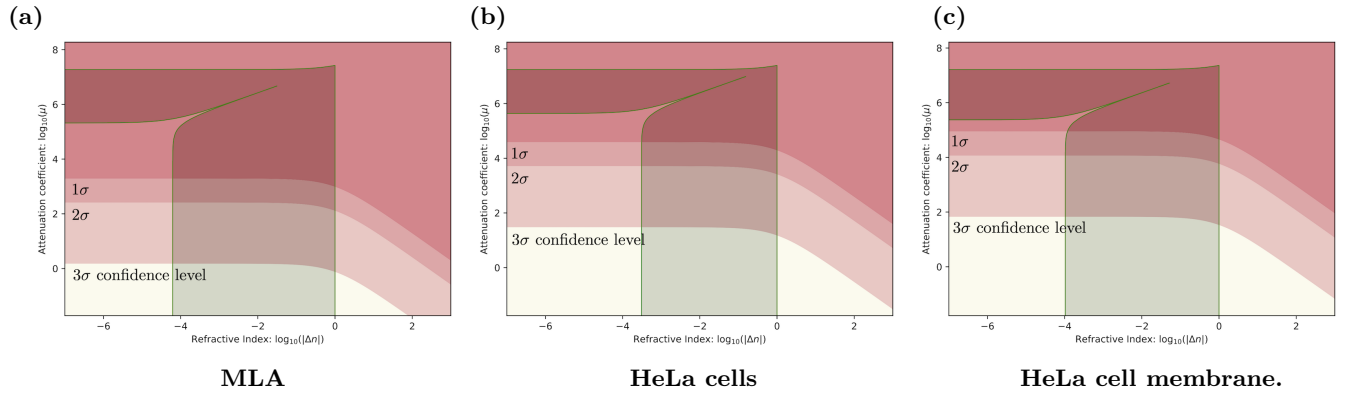
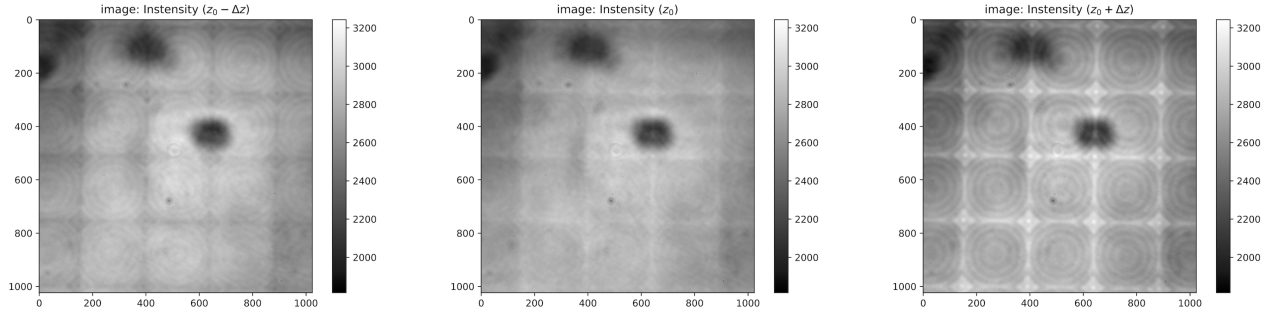


FIG. S2. Parameter allowed regions in the $\Delta n(r_{\perp}, z_0)$ - $\mu(r_{\perp}, z_0)$ spaces: (a) the MLA sample, (b) HeLa cells and (c) HeLa cell membrane. Red contours represent the statistically-allowed regions of the 1σ (68.3%), 2σ (95%) and 3σ (99.7%) confidence intervals. Green area exhibits the physically-allowed region given by the Eq. (10) in the main text.

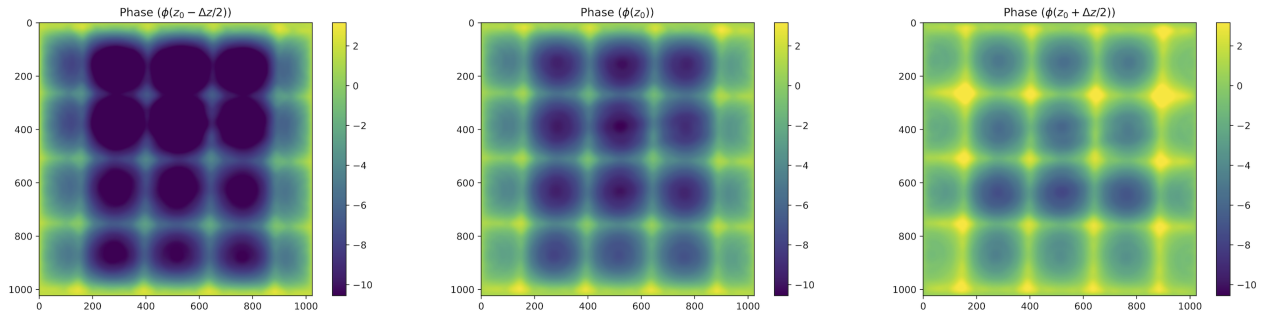
D.2. Reconstruction results

- MLA sample

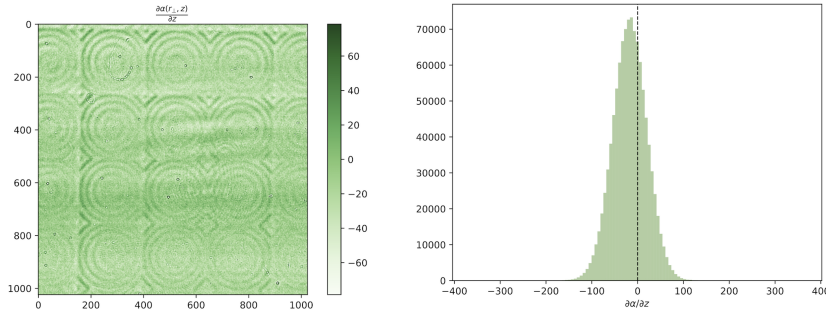
(a) Intensity distributions at $z_0 - \Delta z$, z_0 and $z_0 + \Delta z$



(b) Phase distributions at $z_0 - \Delta z/2$, z_0 and $z_0 + \Delta z/2$



(c) Reconstructed distributions of the $\alpha(r_\perp, z_0)$ -derivative function



(d) Reconstructed distributions of the $\beta(r_\perp, z_0)$ -derivative function

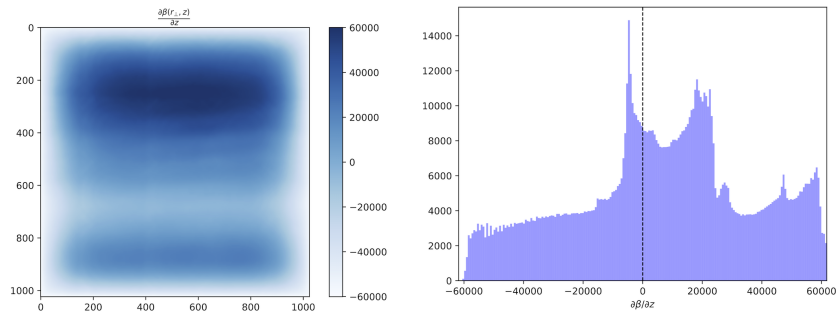
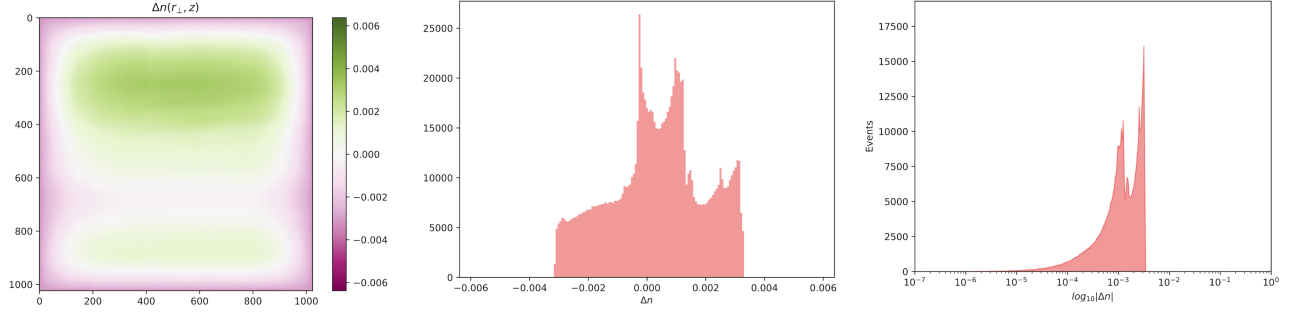
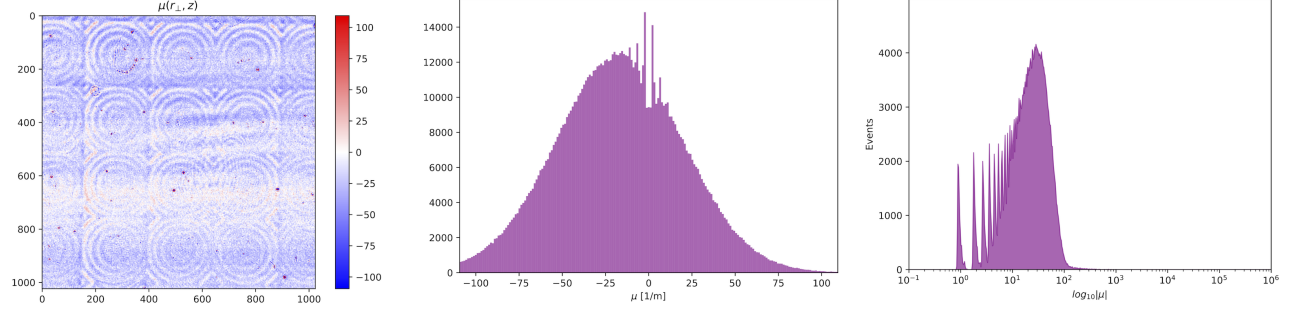


FIG. S3. Results for the MLA sample 1: (a) Intensity distributions, $I(r_\perp, z_0 - \Delta z)$, $I(r_\perp, z_0)$, and $I(r_\perp, z_0 + \Delta z)$. (b) Phase distributions reconstructed from the three fluorescent cell images. (c) Reconstructed distributions of the intensity reduction parameter $\partial_z \alpha(r_\perp, z_0)$ and (d) the phase-coupling parameter $\partial_z \beta(r_\perp, z_0)$.

(e) Reconstructed distributions of refractive-index fluctuations Δx



(f) Reconstructed distributions of attenuation coefficients μ



(g) 2D histogram of Δn and μ

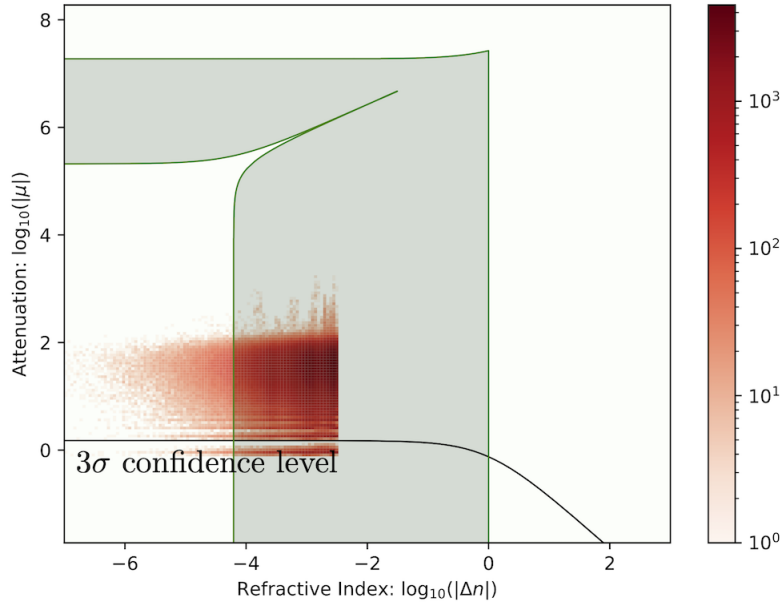
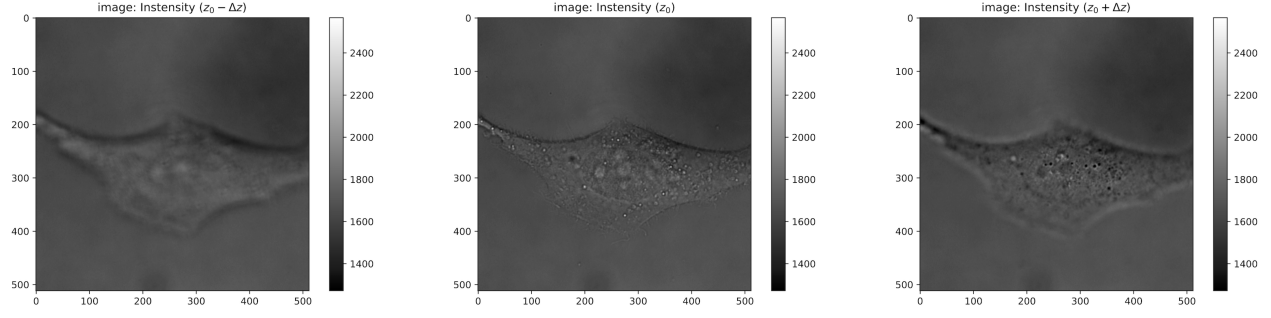


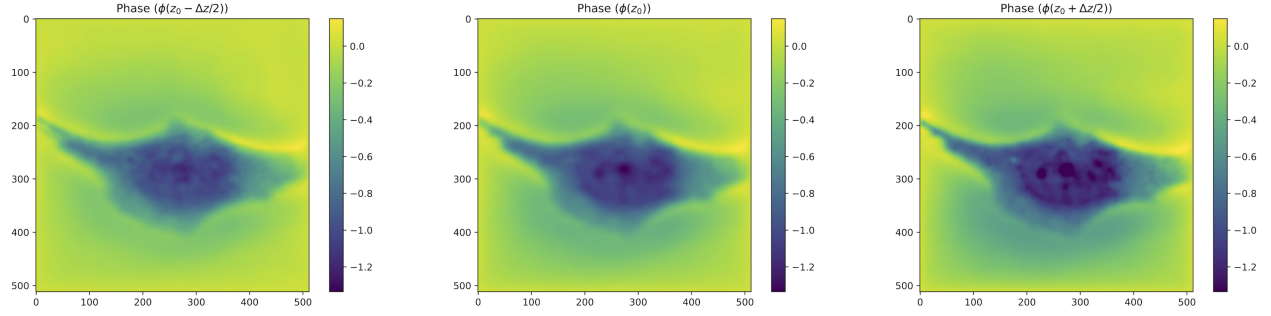
FIG. S4. Results for the MLA sample: (e) Reconstructed distributions and histogram of the refractive-index fluctuations and (f) attenuation coefficients. (g) Correlation pattern between $\Delta n(r_{\perp}, z_0)$ and $\mu(r_{\perp}, z_0)$ lies with the 3σ confidence level (i.e., black solid line). 33,233 events (3.169%) fall outside the physical parameter boundaries (i.e., green area) given by the Eq. (10) in the main text.

- HeLa cell

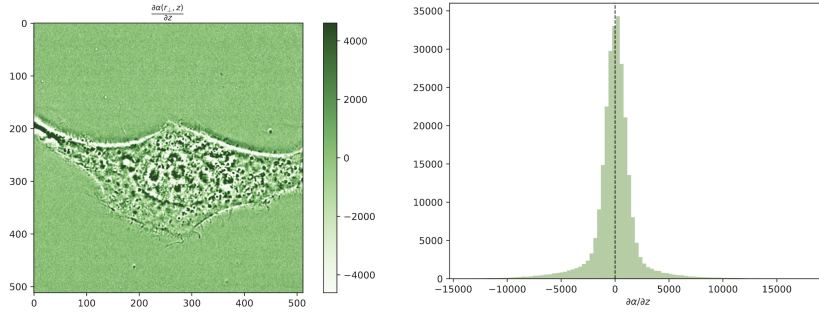
(a) Intensity distributions at $z_0 - \Delta z$, z_0 and $z_0 + \Delta z$



(b) Phase distributions at $z_0 - \Delta z/2$, z_0 and $z_0 + \Delta z/2$



(c) Reconstructed distributions of the $\alpha(r_\perp, z_0)$ -derivative function



(d) Reconstructed distributions of the $\beta(r_\perp, z_0)$ -derivative function

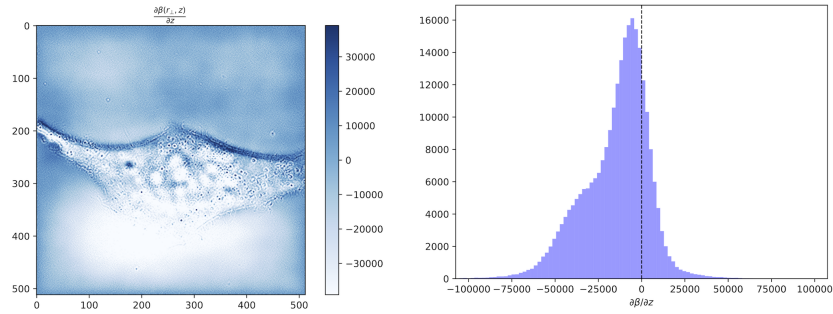
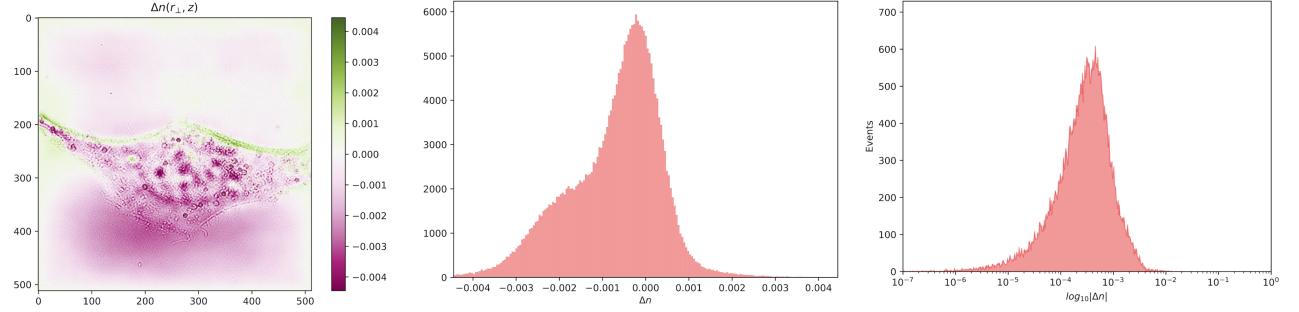
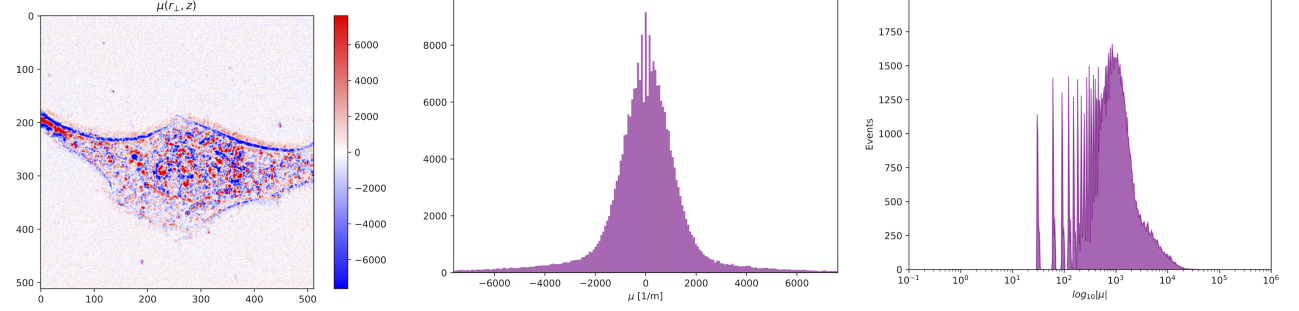


FIG. S5. Results for HeLa cell 1: (a) Intensity distributions, $I(r_\perp, z_0 - \Delta z)$, $I(r_\perp, z_0)$, and $I(r_\perp, z_0 + \Delta z)$. (b) Phase distributions reconstructed from the three fluorescent cell images. (c) Reconstructed distributions of the intensity reduction parameter $\partial_z \alpha(r_\perp, z_0)$ and (d) the phase-coupling parameter $\partial_z \beta(r_\perp, z_0)$.

(e) Reconstructed distributions of refractive-index fluctuations $\Delta n(r_{\perp}, z_0)$



(f) Reconstructed distributions of attenuation coefficients $\mu(r_{\perp}, z_0)$



(g) 2D histogram of $\Delta n(r_{\perp}, z_0)$ and $\mu(r_{\perp}, z_0)$

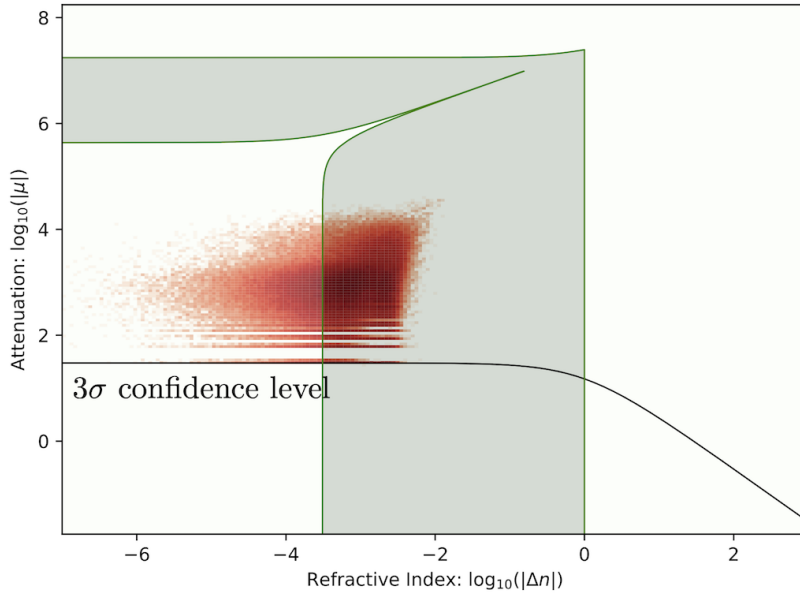
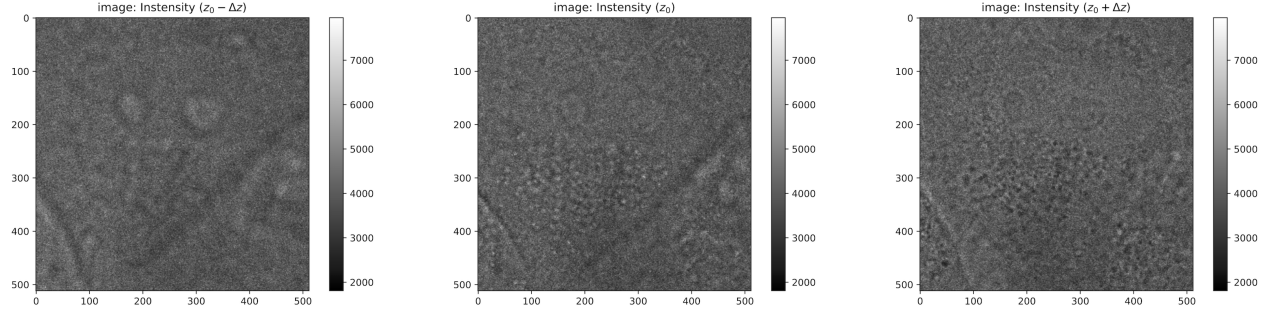


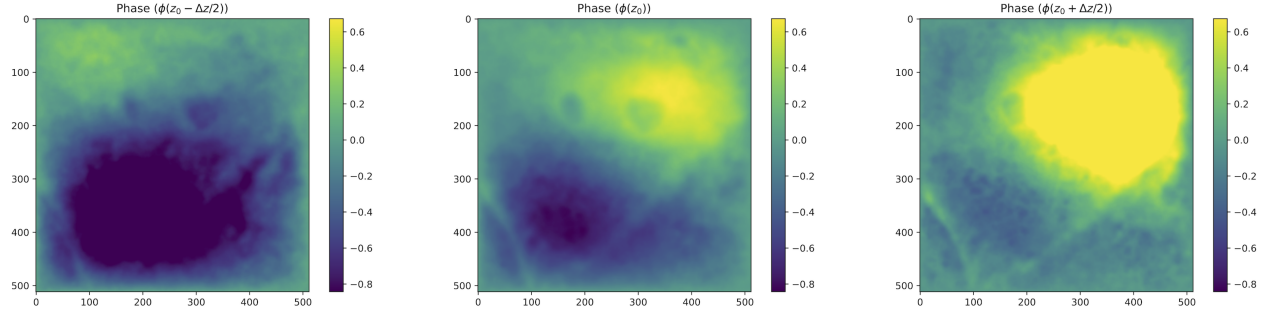
FIG. S6. Results for HeLa cell 2: (e) Reconstructed distributions and histogram of the refractive-index fluctuations and (f) attenuation coefficients. (g) Correlation pattern between $\Delta n(r_{\perp}, z_0)$ and $\mu(r_{\perp}, z_0)$ lies with the 3σ confidence level (i.e., black solid line). 65,055 events (24.82%) fall outside the physical parameter boundaries (i.e., green area) given by the Eq. (10) in the main text.

- HeLa cell membrane

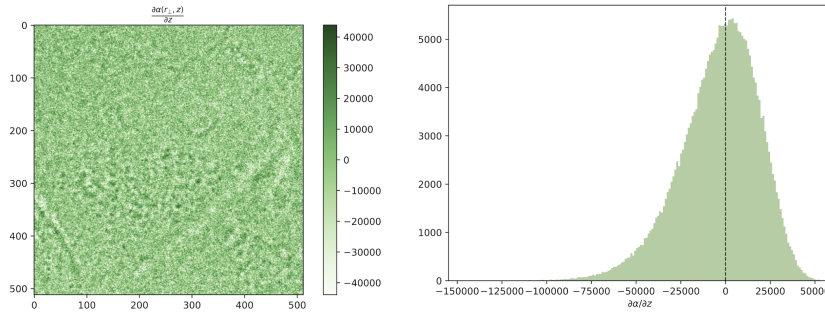
(a) Intensity distributions at $z_0 - \Delta z$, z_0 and $z_0 + \Delta z$



(b) Phase distributions at $z_0 - \Delta z/2$, z_0 and $z_0 + \Delta z/2$



(c) Reconstructed distributions of the $\alpha(r_\perp, z_0)$ -derivative function



(d) Reconstructed distributions of the $\beta(r_\perp, z_0)$ -derivative function

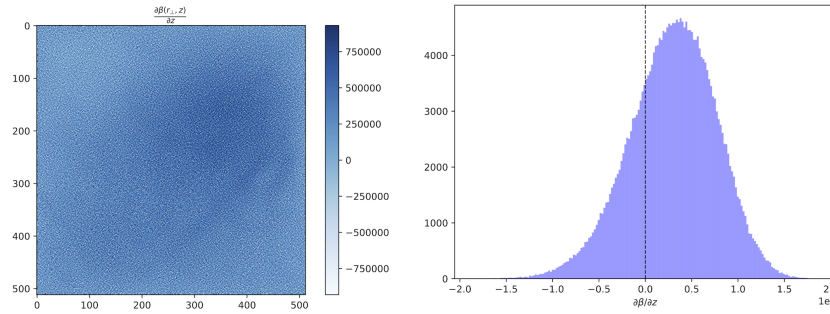
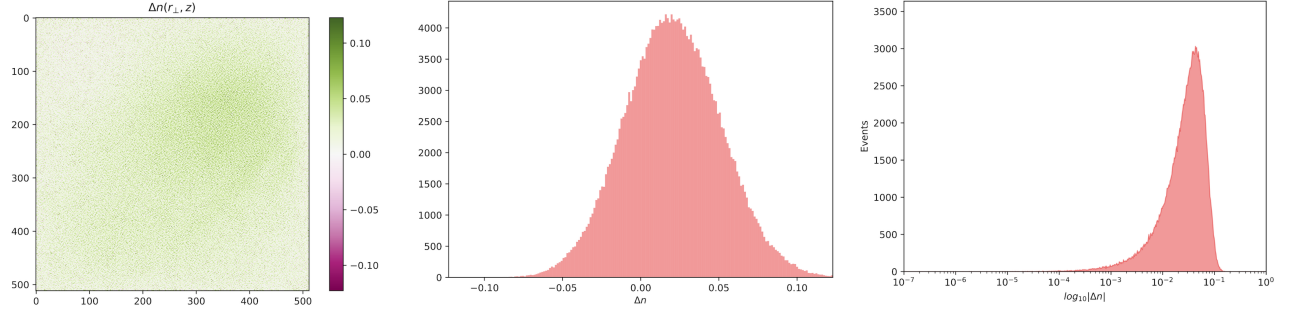
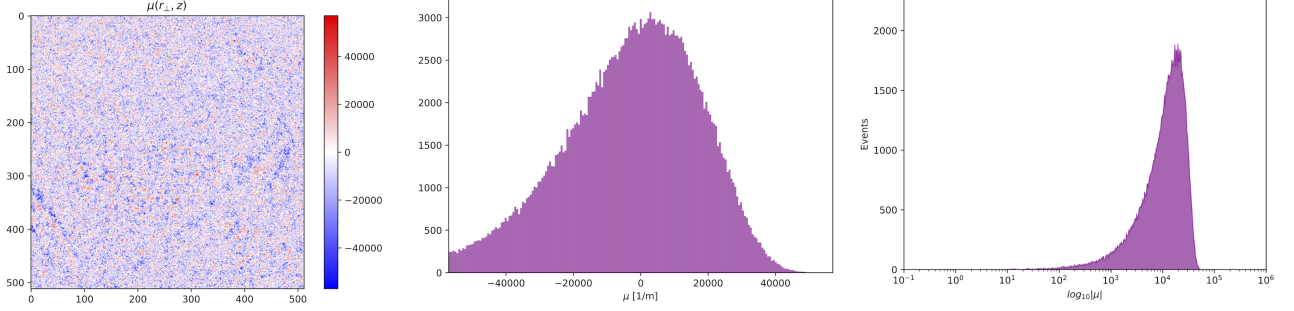


FIG. S7. Results for HeLa cell membrane 1: (a) Intensity distributions, $I(r_\perp, z_0 - \Delta z)$, $I(r_\perp, z_0)$, and $I(r_\perp, z_0 + \Delta z)$. (b) Phase distributions reconstructed from the three fluorescent cell images. (c) Reconstructed distributions of the intensity reduction parameter $\partial_z \alpha(r_\perp, z_0)$ and (d) the phase-coupling parameter $\partial_z \beta(r_\perp, z_0)$.

(e) Reconstructed distributions of refractive-index fluctuations $\Delta n(r_{\perp}, z_0)$



(f) Reconstructed distributions of attenuation coefficients $\mu(r_{\perp}, z_0)$



(g) 2D histogram of $\Delta n(r_{\perp}, z_0)$ and $\mu(r_{\perp}, z_0)$

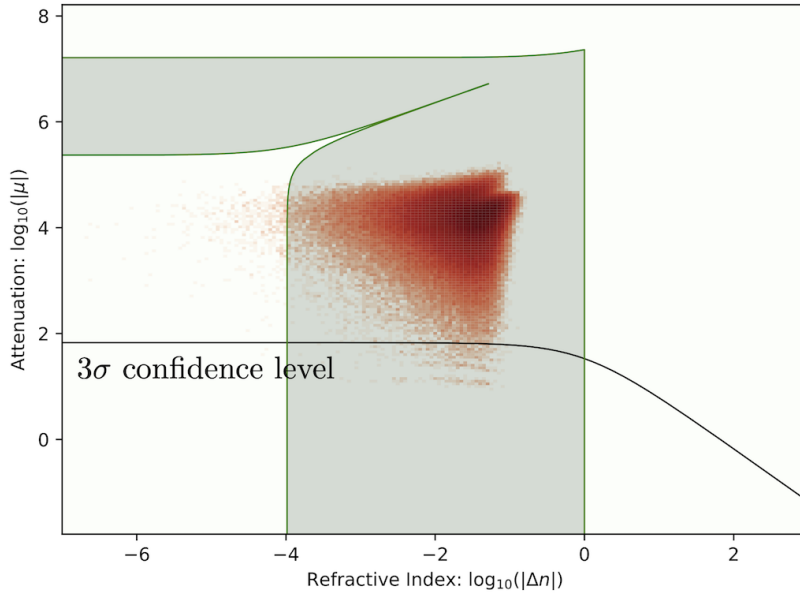
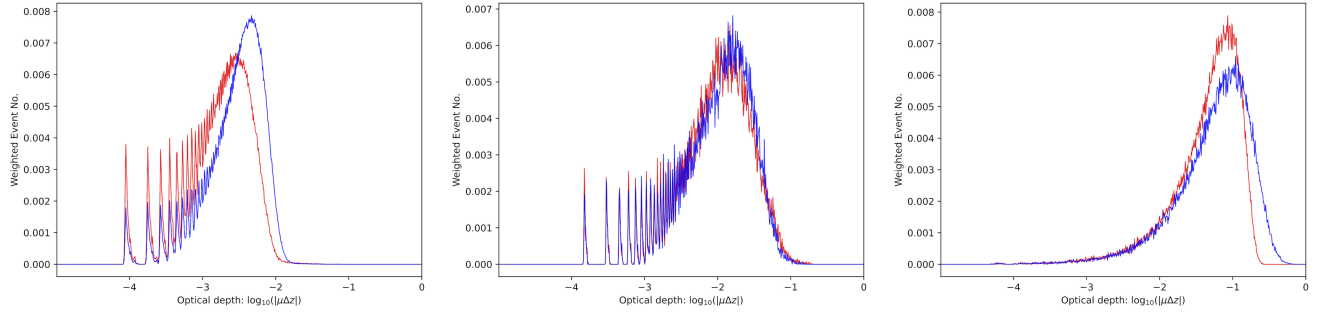


FIG. S8. Results for HeLa cell membrane 2: (e) Reconstructed distributions and histogram of the refractive-index fluctuations and (f) attenuation coefficients. (g) Correlation pattern between $\Delta n(r_{\perp}, z_0)$ and $\mu(r_{\perp}, z_0)$ lies with the 3σ confidence level (i.e., black solid line). 555 events (0.217%) fall outside the physical parameter boundaries (i.e., green area) given by the Eq. (10) in the main text.

D.3. Results of symmetry analysis

(a) Propagation probability



(b) Asymmetry property

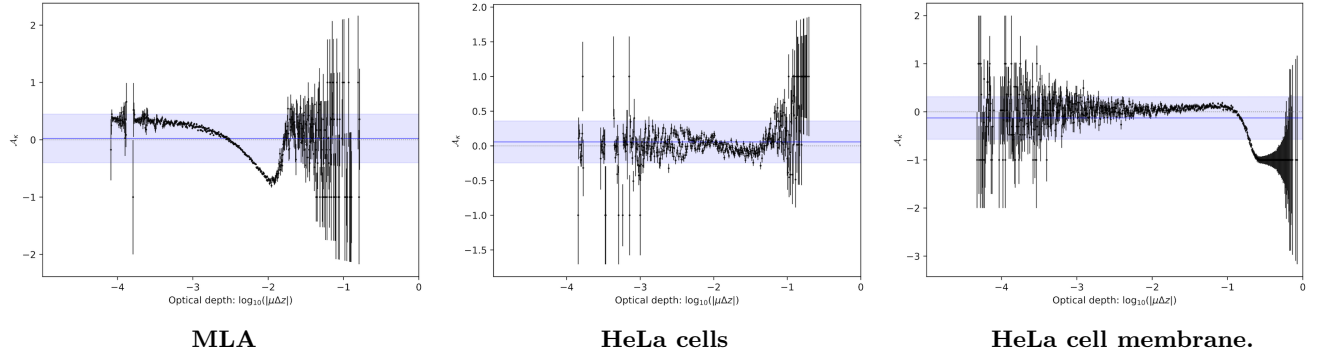


FIG. S9. Results of symmetry analysis. (a) Histograms of propagation probabilities as a function of optical depth. Red and blue lines in the histograms denote the propagation probabilities in forward and backward directions, respectively. (b) Asymmetry property as a function of optical depth. Blue line and bands in the asymmetry property plots are the statistical average and the root mean squared (RMS) value, respectively. Dashed line represents $\mathcal{A}_\kappa = 0$.